Spatiotemporal characteristics and filament interaction in femtosecond Hermite-Gaussian laser pulses in a gas

Zhanxin Wang, Jiansheng Liu, Haiyi Sun, and Zhizhan Xu

Phys. Rev. A **87**, 053816 — Published 13 May 2013

DOI: 10.1103/PhysRevA.87.053816

Spatiotemporal characteristics and filament interaction in femtosecond Hermite-Gaussian laser pulses in a gas

Zhanxin Wang,[1,2] Jiansheng Liu,[1,*] Haiyi Sun,[1] and Zhizhan Xu[1,†]

[1]*State Key Laboratory of High Field Laser Physics, Shanghai Institute of Optics and Fine Mechanics, Chinese Academy of Sciences, P.O. Box 800-211, Shanghai 201800, China*

[2]*School of Physics and Electronic Engineering, Jiangsu Normal University, Xuzhou 221116, China*

(Dated: April 23, 2013)

Abstract

In this contribution, we investigate the femtosecond filament interactions in gas by employing Hermite-Gaussian TEM_{02} mode focused by lens in argon gas by means of numerically evaluating the $3+1$ dimension nonlinear Schrödinger equation. High-resolution spatio-temporal characteristics has been obtained. The TEM_{02} mode laser pulse, which has three lobes in the plane perpendicular to the propagation direction, can form three filaments. In the filamentation region, interaction between the lobes occurs at the trailing parts of the laser filaments where correspond to the blueshifted supercontinuum generated by self-phase modulation and plasma. We find the energetic spatio-temporal fragments are more inclined to repulsion rather than fusion when close to each other, which may imply that two adjacent single filaments dislike to combine into a 'big filament' in multi-filaments. It seems that the phenomenon of repulsion bears no relation to the phase difference between the input sub-pulses. Our finding may help to understand why one cannot supply energy to single filament by multi-filaments fusion until to now.

PACS numbers: 42.65.Jx, 42.65.Re, 32.80.Wr, 42.68.Ay

* michaeljs_liu@mail.siom.ac.cn

† zzxu@mail.shcnc.cn

I. INTRODUCTION

It has been for nearly twenty years since the first experimental observation of femtosecond laser self-channeling by Braun *et* al. in 1995 [1], which is commonly accepted as the beginning of modern filamentation optics science. However, femtosecond filamentation is still a very active research field in strong-field science (see the list of publications [2]), which, in our opinion, mainly benefits from the abundant and diverse nonlinear dynamics in the filaments and consequent many novel phenomena and potential applications. As far as the numerical simulation is concerned, the radially-symmetrical nonlinear Schrödinger equation (2D+1 NLS) as a main tool describing the propagation phenomena has been solved many times and still being solved currently due to its less computational demand and its proved potential ability to tackle many basic problem. However, to be limited by the axis-symmetrical requirement of 2D+1 NLS, some more generally existing non-axisymmetric or symmetry-breaking propagation problems still need to numerically solve the full three space-dimensional nonlinear Schrödinger equation (3D+1 NLS). There have been some examples [3–14], amidst which the filament interaction [10–13] and multi-filamentation competition [3–8] are two traditional themes that need to use the 3D+1 NLS.

In the aspect of filaments interaction, some early studies [15] use laser beams instead of pulse. Although the authors also use the word of 'filament' instead of 'self-trapping beam', the filament is actually different from the concept of femtosecond laser filaments now widely accepted. Thus the details of interaction in temporal domain can not be obtained. Xi *et* al [11] have published a paper on spatio-temporal interaction of filaments in 2006, where every case such as attraction, fusion, repulsion, and spiral propagation has been discussed by assuming a constant phase difference between two filaments' envelope from the viewpoint of interference. However, the phase in the filaments is both frequency- and space-dependent, which therefore results that the constant phase difference do not appear to in the actual filaments interaction.

In this contribution, we investigate the filaments interaction from some spatio-temporal details aspects by considering the nonlinear propagation of femtosecond TEM_{02} mode Hermite-Gaussian(HG) laser pulse using high-resolution grids in (3+1) dimension numerical simulation. The TEM_{02} mode has three lobes in the plane perpendicular to the propagation direction, which will produce three filaments and interact with each other when focusing by lens. we find that the energetic spatio-temporal fragments are more inclined to repulsion rather than fusion when close to each other. The repulsion eventually results the pulse splits into many spatio-temporal

fragments.

This paper is organized as follows. In Sec. II, we provide a overview of the nonlinear propagation model and the numerical technique to evaluate it. In Sec. III, we discuss the details on TEM_{02} mode HG femtosecond laser pulse. our results are briefly summarized in Sec. IV. In the appendix, we provide the code structure used to numerically evaluate 3D+1 NLS in parallel.

II. PHYSICAL MODELS AND NUMERICAL TECHNIQUE

The HG transverse mode can be generated from the laser's optical resonator which is designed radially asymmetrically [16]. The linear propagation of monochromatic HG beam has been widely investigated. Siegman [16] has given a analytical expression on the linear propagation of monochromatic HG beam focused in media, which show the beam preserve its HG profile during propagation. The result also indicated there exists no interaction among the different lobes of HG beam. Siegman's analytical formula cannot be applied to the propagation of laser pulse with HG transverse mode due to the existence of dispersion. Especially, when the laser pulse is enough strong, the nonlinear effects due to self-focusing and plasma generation by media ionization will break its original HG profile, even cause interaction between the different lobes.

Considering a linearly polarized femtosecond transform-limited laser pulse with HG transverse TEM_{20} mode with Gaussian temporal profile focused by a lens in argon under the standard atmospheric pressure. Its electric field $\varepsilon_0 \equiv \varepsilon_0(x, y, t)$ can be described as

$$\varepsilon_0 = A_0(\frac{8x^2}{w_0^2} - 2)\exp(-\frac{x^2+y^2}{w_0^2})\exp(-\frac{t^2}{T_0^2} - i\omega_0 t). \tag{1}$$

After the lens, the spectra $\widetilde{\varepsilon_0} \equiv \widetilde{\varepsilon_0}(x, y, \omega)$ of its electric field at the plane immediately behind the lens can be expressed as

$$\begin{aligned}\widetilde{\varepsilon_0} = & \sqrt{\pi}T_0 A_0(8x^2/w_0^2 - 2)\exp[-(x^2+y^2)/w_0^2] \\ & \times\exp[-i\omega(x^2+y^2)/2cf]\exp[-T_0^2(\omega-\omega_0)^2/4],\end{aligned} \tag{2}$$

where $T_0 = 25.4$ fs is the pulse duration (corresponds to $t_{FWHM} \simeq 30$ fs), $w_0 = 4$ mm is the spot size, c is the light speed in vacuum, $\omega_0 = 2.36$ PHz is the laser carrier frequency (wavelength $\lambda_0 = 800$ nm), $f = 1$ m is the focal length, $A_0 = 3.287 \times 10^7$ V/m is the electric field amplitude (corresponds to pulse energy ~ 6.9 mJ). The parameter values are used in the simulations also shown above together. The relationships among the amplitude A_0, peak power P, and energy E of

the TEM_{20} mode Gaussian laser pulse are $P = 4\pi w_0^2 A_0^2$ and $E = 8(\pi/2)^{3/2} w_0^2 T_0^2 A_0^2$, respectively. The Fourier transformation and its reverse used in this paper between the electric field ε and its spectra $\widetilde{\varepsilon}$ are defined as $\widetilde{\varepsilon} = \int_{-\infty}^{+\infty} \varepsilon e^{i\omega t} dt$ and $\varepsilon = (1/2\pi) \int_{-\infty}^{+\infty} \widetilde{\varepsilon} e^{-i\omega t} d\omega$ respectively. In terms of Eq. (2), we can see that the HG mode laser pulse preserves its original intensity profile for each frequency component at the plane immediately behind the lens, which show the focusing effect caused by lens do not change the beam mode although a position-dependent phase-shift has been added.

The unidirectional propagation model picturing the spectra of electric field in the group-velocity moving reference frame can be expressed as [17]

$$\partial_z \widetilde{\varepsilon} = \frac{i}{2k(\omega)} \nabla_\perp^2 \widetilde{\varepsilon} + i\widetilde{D}(\omega)\widetilde{\varepsilon} + \frac{i\mu_0 \omega^2}{2k(\omega)} \widetilde{F}_{NL}, \tag{3}$$

where $\widetilde{\varepsilon}$ is the spectra of electric field, $\widetilde{F}_{NL} = \widetilde{P}_{NL} + i\widetilde{J}/\omega$ describes the nonlinearity containing the Kerr nonlinear polarization P_{NL} and the current density J. $\widetilde{D}(\omega) = k(\omega) - k^{(0)} - k^{(1)} = \Sigma_{n=2}^{\infty}(k^{(n)}/n!)(\omega - \omega_0)^n$ describes the chromatic dispersion with $k^{(0)} = n_0\omega_0/c$ and $k^{(n)} = (d^n k(\omega)/d\omega^n)_{\omega=\omega_0}$. Here we have drop the (x, y, z, ω) dependence of $(\widetilde{\varepsilon}, \widetilde{F}_{NL}, \widetilde{P}_{NL}, \widetilde{J})$ and (x, y, z, t) dependence of (P_{NL}, J) for clarity. The plasma density $\rho \equiv \rho(x, y, z, t)$ is described as

$$\partial_t \rho = W(|\varepsilon|^2)(\rho_{\mathrm{nt}} - \rho) + \sigma\rho|\varepsilon|^2/I_p, \tag{4}$$

where the ionization rate $W(|\varepsilon|^2)$ is evaluated by multi-photon ionization models, I_p is the atomic ionization potential of argon and σ is the cascade ionization rate. The parameters for argon used in our simulation have been listed in the recent reference [19].

To directly or split-step evaluate the Eq. (3) combining with Eq. (4), the widely used methods are the finite difference method [20] and the fourth-order Runge Kutta (RK4) method [17]. This two kind of methods have almost the same calculation speed in the evaluation of 2D+1 NLS and both can be generalized to evaluate the 3D+1 NLS, however, the RK4 method need in principle to calculate the electron density four times in every propagation step comparing to the finite difference method which just calculate the electron density one time in every step. In the case of 2D+1 NLS, the electron density is evaluated very fast, however, the CPU time will increase in the evaluation of 3D+1 NLS due the repetitive calculations of electron density. Of course, we also can just evaluate the electron density one time in every step in the RK4 method, which in fact do not cause error. Here we numerically evaluated the Eq. (3) using the alternating direction implicit (ADI) Peaceman-Rachford finite difference scheme, which read as follows [21]:

For every discretized laser frequency ω_i from ω_{min} to ω_{max}, we evaluated the propagation of the discretized electric-field spectra $\widetilde{\varepsilon}_{j,k}^{n+1} \equiv \widetilde{\varepsilon}(j\Delta x, k\Delta y, (n+1)\Delta z)$ from $n\Delta z$ to $(n+1)\Delta z$ by two half-steps. The first half-step with step-size $\Delta z/2$ corresponding to x-implicit and y-explicit read as

$$\begin{aligned} -D_x\widetilde{\varepsilon}_{j-1,k}^{n+1/2} + (1+2D_x-D_l)\widetilde{\varepsilon}_{j,k}^{n+1/2} - D_x\widetilde{\varepsilon}_{j+1,k}^{n+1/2} \\ = D_y\widetilde{\varepsilon}_{j,k-1}^{n} + (1-2D_y+D_l)\widetilde{\varepsilon}_{j,k}^{n} + D_y\widetilde{\varepsilon}_{j,k+1}^{n} \\ +\delta_l(3\widetilde{F}_{j,k}^{n} - \widetilde{F}_{j,k}^{n-1/2}), \end{aligned} \tag{5}$$

and the second half-step with step-size $\Delta z/2$ corresponding to y-implicit and x-explicit read as

$$\begin{aligned} -D_y\widetilde{\varepsilon}_{j-1,k}^{n+1} + (1+2D_y-D_l)\widetilde{\varepsilon}_{j,k}^{n+1} - D_y\widetilde{\varepsilon}_{j+1,k}^{n+1} \\ = D_x\widetilde{\varepsilon}_{j,k-1}^{n+1/2} + (1-2D_x+D_l)\widetilde{\varepsilon}_{j,k}^{n+1/2} + D_x\widetilde{\varepsilon}_{j,k+1}^{n+1/2} \\ +\delta_l(3\widetilde{F}_{j,k}^{n+1/2} - \widetilde{F}_{j,k}^{n}). \end{aligned} \tag{6}$$

Where the coefficients are defined as $D_x = i\Delta z/(4k(\omega_i)\Delta x^2)$, $D_y = i\Delta z/(4k(\omega_i)\Delta y^2)$, $D_l = i\Delta z\widetilde{D}(\omega_i)/4$, and $\delta_l = i\mu_0\omega_i^2\Delta z/(8k(\omega_i))$ respectively, and Δx and Δy are the grid-spacing in the x and y orientations respectively. The nonlinear term is discreted by Adams-Bashforth scheme [21] as has been used by Couairon *et* al. [20]. We use intensity-dependent propagation step-size $\Delta z_n = \Delta z_0 I_0/I_n$. Here I_0 and I_n are the peak intensity of the initial and the nth step, respectively.

Our code based on the numerical scheme shown above is run on a desktop workstation with two Intel Xeon E5620 CPUs. The higher computational efficiency comes from the combination of OpenMP parallel computing techniques with the usage of single-precision number instead of double-precision number generally used in the evaluation of 2D+1 NLS. The reasonability to use single-precision number has been justified by our 2D+1 code. For the details of the code, please see the Appendix.

III. NUMERICAL RESULTS AND DISCUSSION

In this section, we will discuss the propagation of TEM_{02} mode laser pulse in argon. Considering the complete 3D+1 dimensional numerical simulation can be very time-consuming, however, one always hope higher resolution can be obtained by using space-time grid of limited numbers. During the simulation, the larger is the light spot, the more spatial grids are needed. Therefore, our trick is that we replace the nonlinear propagation by linear propagation in the region near the back

plane of the lens and far away from the focus point where the laser intensity is relatively low to it in the filaments. this original idea comes from the fact that the linear propagation of TEM_{02} mode pulse can be evaluated analytically and a pulse with smaller light spot can be obtained due to the existence of focusing by lens. Therefore, in the following, we will firstly carry through our numerical experiments following this strategy. We evaluate the pulse propagation by two steps, in which from the lens to 85 cm distant from the lens we analytically evaluate the linear propagation equation by neglecting the nonlinear terms in Eq. (3), and then from 85 cm to the energy exhaustion of the pulse we numerically evaluate the Eq. (3). Of course, as a comparison, we will finally give the nonlinear propagation characteristics from directly numerically evaluating the Eq. (3) from the lens up to the energy exhaustion of the pulse. The numerical experiment is sketched in Fig. 1.

Therefore, let's give a overview of the linear propagation of the TEM_{02} laser pulse formulated by Eq. (2). When neglected the nonlinear term F_{NL} including Kerr and plasma effects, the propagation equation Eq. (3) is reduced to

$$\partial_z \widetilde{\varepsilon} = [i/2k(\omega)]\nabla_\perp^2 \widetilde{\varepsilon} + i\widetilde{D}(\omega)\widetilde{\varepsilon}. \tag{7}$$

To help express the obtained results, we establish a reference frame where the pulse propagates along the z-axis direction, and select the linear focus of the lens as the origin of coordinates (the reference frame be used below). In this way, after tedious but simple calculation, we can express analytically the spectra of electric field in the position z in terms of Eq. (2) and Eq. (7) as

$$\begin{aligned}\widetilde{\varepsilon}(z) = \frac{\sqrt{\pi}T_0A_0}{4pq}\Big(&\frac{x^2}{2p^2q^2w_0^2} - \frac{1}{p^2w_0^2q} + \frac{4}{pw_0^2} - 2\Big)\\ &\times\exp\Big(-\frac{x^2+y^2}{4q}\Big)\exp\Big[-\frac{(\omega-\omega_0)^2T_0^2}{4}\Big]\\ &\times\exp[i\widetilde{D}(\omega)(f+z)],\end{aligned} \tag{8}$$

where $p = 1/w_0^2 + ik(\omega)/(2f)$ and $q = 1/(4p) + i(f+z)/[2k(\omega)]$. In this case, each frequency component still preserves its HG intensity profile. In terms of Eq. (8), we note that the dispersion effect is relative small before the focal plane of the lens due to short propagation distance.

We firstly give a discussion on the difference between our analytical approximation and the direct evaluation of Eq. (3). Figs. 2(a,b) show respectively the spatio-temporal intensity distribution in x-t plane (where $y = 0$. The following is same if not specified) and y-t plane (where $x = 0$. The following is same if not specified) corresponding to the position immediately behind the lens where $z = -100$ cm, which are plotted in terms of Eq. (2). Obviously, the wavefront is

severely curved by the lens. In the *x*-*t* plane, the two side-lobes' peak intensity is ~ 0.57 TW/cm^2 located at (± 4.47 mm, -33.5 fs), and the center-lobe's peak intensity is ~ 0.43 TW/cm^2 located at (0 mm, 0 fs). The pulse durations of the side-lobe and the center lobe are both ~ 30.3 fs (be evaluated in terms of the position of its peak intensity). The *y*-*t* plane show the same data as in *x*-*t* plane but just corresponding to the center-lobe. Figs. 2(d,e) show the corresponding intensity distribution as in Figs. 2(a,b) in the distance 85.3 cm behind the lens where $z = -14.7$ cm, which are plotted in terms of the analytical formula Eq. (8). The curve degree of the wavefront has been alleviated evidently. The peak intensities of the center-lobe and side-lobe are 17.8 TW/cm^2 and 23.4 TW/cm^2, and located at (0 mm, -1.2 fs) and (-0.66 mm, -6.0 fs), respectively, in the *x*-*t* plane. The corresponding pulse duration for the lobes are both 30.7 fs. Compared Fig. 2(a) with Fig. 2(d), a small temporal offset from 0 fs to -1.2 fs in the center-lobe comes into our notice. The offset will accumulate with the increase of propagation distance. what cause this offset since we use group-velocity reference? The answer is higher-order dispersions than the second-order! In fact, if we replace the $\widetilde{D}(\omega)$ in Eq. (8) which include dispersion of all orders by $(k^{(2)}/2)(\omega - \omega_0)^2$, the offset disappears immediately. To evaluate the effect of dispersion on the tightly focusing linear propagation, we compare the Fig. 2(a) with Fig. 2(d) and find it broaden the pulse ~ 0.4 fs and offset the pulse ~ -1.2 fs from the temporal center. This is actually a so small effect that can be neglected completely.

However, even in the low-intensity region, the self-focusing and ionization still exist, and may produce important effects. Figs. 2(g,h) also show the spatio-temporal intensity distribution at the position of $z = -14.7$ exactly the same as in Figs. 2(d,e), but obtained by numerically evaluating the nonlinear Eq. (3) from the initial condition expressed by Eq. (2). The peak intensities in the *x*-*t* plane corresponding to center-lobe and side-lobe are 26.5 TW/cm^2 and 19.6 TW/cm^2, and located at (0 mm, 29.1 fs) and (-0.73 mm, -4.8 fs) in the *x*-*t* plane, respectively. the different offsets from in Figs. 2(d,e) may come from the slight self-phase modulation (SPM) and plasma generation.

A significant difference between Fig. 2(d) and Fig. 2(g) lies in the relative intensity between the center lobe and the side-lobe. In the initial position where $z = -100$, the side-lobe's peak intensity is higher than the center-lobe, and the ratio of the two intensity is ~ 1.32. In the case of linear propagation, this ratio is preserved. However, as we have seen from Fig. 2(g), in the actual nonlinear propagation evaluated by directly solving Eq. (3), the center-lobe's peak intensity even have greatly exceeded the side-lobe's. Fig. 3 explains this phenomenon. As shown in Fig. 3, for the focusing effect caused by lens, the three lobes both focus toward the lens' foci; however, for

the self-focusing effect produced by the media's intensity-dependent refractive index $n = n_0 + n_2|\varepsilon(x, y, z, t)|^2$ where $|\varepsilon(x, y, z, t)|^2$ is the intensity of the laser pulse, the self-focusing in every lobe is toward its own intensity center as shown in Fig. 3. Thus, for the center-lobe, the self-focusing will enhance the focusing caused by lens, while for the side-lobe, the two focusing effects even cut down each other, which is clear by comparing the data shown in Figs. 2(d,g).

In the following, let us begin to look at the nonlinear characteristics and interaction in the filamentation region at length. Our discussion is qualitative. Fig. 4 shows the spatio-temporal intensity distribution in the x-t and y-t planes respectively in the distance of $z = -8.8, -7.0, -2.6$ cm, where corresponds to the fore-, mid-, and post-filamentation region respectively. The corresponding fluence distributions in the x-y plane in the three positions are shown in Fig. 5. we firstly take notice that the original symmetry in spatial direction is preserved very well, which also show good stability in our code. These figures are plotted in terms of our approximation model. We use $1024 \times 768 \times 4096$ grid numbers in the x, y, and t directions with window-size $1.5w_0$, $1.5w_0$, and $32T_0$, respectively.

Figure 4(a) shows the three lobes firstly independently suffer intensity clamping and plasma defocusing in its trailing part in the early stage of filamentation, and form into approximative hollow cone-shaped spatio-temporal dynamics, which is highly similar to the 2 + 1 dimensional case of radial symmetry propagation for each lobes alone ([18, 19]). The fluence shown in Fig. 5(c) confirms there exist no interaction between the lobes in this stage. With further propagation, the hollow cones continue to expand and close to each other from the trailing part as shown in Fig. 4(b). Interestingly, it seems that these approaching energetic parts are not willing to fuse each other together but are more inclined to repulse each other, which also can be clearly seen from Fig. 5(d) on both side of position $x = \pm 0.25$ mm where the energy is accumulated due to the repulsion. Ultimately, many spatial-temporal energetic fragments was formed as shown in Fig. 4(c) due to the repulsion interaction among each other. we note that the repulsion even result in a kind of "squeeze effect" on the center lobe by the two side-lobes, and therefore its energy diffusion in the x-direction is limited and therefore ejected its energy mainly toward the y-direction. By Comparing Fig. 4(e) with Fig. 4(f), we clearly see this expansion effect. More clear observation about the repulsion dynamics can be obtained from our supplementary media files (.GIF files).

As a comparison, let us briefly discuss the dynamics obtained by directly evaluating the nonlinear Eq. (3) from initial condition Eq. (2). To give better spatial resolution, we use $1536 \times$

1024×4096 grid numbers in the x, y, and t directions with window-size $4.5w_0$, $4.0w_0$, and $32T_0$, respectively (The resolution is still lower than the approximation model). We have to select larger window due to the large light spot size. Fig. 6 shows the spatio-temporal intensity distribution in the x-t plane and y-t plane, respectively, in the typical filamentation region. The dynamics is in fact qualitatively similar to the result shown in Fig. 4. The three lobes firstly filament independently without interaction, then the trailing parts close to each other due to further plasma defocusing, and then repulsively interact, and also form complicated spatio-temporal structures. we notes that the repulsion effect still exist clearly, however, further details cannot be well distinguished. In this case, the ejection effect in y-direction is weakened due to earlier filamentation of center-lobe results in consumption of partial energy due to ionization.

Generally, it is believed that the phenomena such as repulsion and fusion in the filament interaction are related to the initial relative phase difference between the sub-pulses or filaments of interaction. Bergé *et* al. [15] have shown that two beamlets with opposite phases will never coalesce, but two in-phase beamlets will rapidly collapse toward their respective centers without interaction due to the lack of defocusing mechanism if their initial powers are higher than the threshold for self-focusing. In the beamlets case, especially when their powers are lower than the threshold for self-focusing, their spectra and relative phase will not change along the propagation direction for lack of temporal configuration, thus, it seems that the interaction is similar with the interference of two single-color or multi-color beams. Further, for two light bullets with determinate phase difference, Xi *et* al. [11] showed the similar interaction and explained it from the viewpoint of interference.

In our case, there is not an overall constant phase difference between the side-lobe and center-lobe during filamentation. The relative phase shift is both position- and frequency-dependent. Fig. 7(a,b) show Spatio-temporal intensity distribution in the x-t plane and the correponding spectral intensity distribution in the x-ω plane at the typical distance of $z = -9.34$ cm before the interaction appears. Since the interaction appears in their edges of the lobes, we also show the spectral phase in their edges. Fig. 7(c,d) show the spectral phase at $x = -0.1$ mm and $x = -0.3$ mm as marked in Fig. 7(b) by dashed line, and it is limited to the range from 0 to 2π. The spectral phase approximates to parabolic shape due to the second-order dispersion. We find their phase difference is close to 0, and the phase difference keeps almost fixed until their interaction appears. This suggests the two filaments are in-phase. Similarly, Fig. 8 shows the spectral intensity and phase at $z = -7.0$ cm corresponding to Fig. 4(b) where the repulsion effect has appeared. the

phase difference between the two interaction edges becomes to $\pi/2$, but the spectra have been slightly blue-shifted due to self-phase modulation or plasma, and the phase has also deviated from the parabolic shape. In addition, from the simple viewpoint of interference, even if two frequency components have phase difference of $\pi/2$, their superposition still should enhance the intensity. However, in our case, the spectra intensity between the two interaction filaments is about two orders of magnitude lower than the peak spectral intensity as shown in Fig. 8(c). Therefore, we think that, during filaments interaction, the main role is played by the dynamic processes such as focusing and defocusing effects rather than the static interference effect.

IV. CONCLUSIONS

In summary, we numerically investigate the linear and nonlinear propagation of TEM_{02} mode femtosecond HG laser pulse tightly focused in argon. For the case of linear propagation, we give an analytical expression. Our important point is placed on its nonlinear propagation to investigate the interaction between its lobes. High-resolution spatio-temporal dynamics in the filamentation has been shown. We find the interaction between the different lobes mainly appear in the trailing part of the pulse due to the plasma defocusing, and when the energetic parts of different lobes close to each other, it is more inclined to repulse each other rather than fusion. Our finding may help to understand why one cannot supply energy to single filament by multi-filaments fusion until to now. For the mechanism of the filament interaction especially in the trailing part, we think it may come from the defocusing mechanism. Qualitatively, intensity-clamping can help to understand the repulsion effect. Of course, considering the laser pulse and the filament as a coherent light source, the interference phenomena may exist during filaments interaction, however we do not think it plays the main role when the filaments repulse each other.

Appendix: The code structure for 3D+1 NLS

The appendix shows the details of our code structure for numerical solution of $3+1$ dimension nonlinear schrödinger equation. The annotate makes use of Fortran style. the following is the code:

PROGRAM 3D_NLS

define x-grid $(-M_x/2+1, \cdots, M_x/2)\Delta x$

define y-grid $(-M_y/2+1,\cdots,M_y/2)\Delta y$

define t-grid $(-M_t/2+1,\cdots,M_t/2)\Delta t$

define ω-grid $(0,\cdots,M_t/2,-M_t/2+1,\cdots,-1)\Delta\omega$

! note that $\Delta\omega\Delta t = 2\pi/M_t$

define initial condition $\varepsilon(x,y,t)$ or $\widetilde{\varepsilon}(x,y,\omega)$

DO $z = z_1, z_{max}$

PARALLEL DO $x = x_{min}, x_{max}$

DO $y = y_{min}, y_{max}$

calculate electron density $\rho(x,y,:)$! : denote t

! evaluate Eq. (4) by second-order Runge-Kutta scheme

calculate nonlinear term $\widetilde{F}_{NL_2}(x,y,:)$! : denote ω

END DO (y)

END PARALLEL DO (x)

PARALLEL DO $\omega = \omega_{min}, \omega_{max}$

calculate spectra $\widetilde{\varepsilon}(x,y,\omega)$ by Eq. (5) !stepsize= $\Delta z/2$

END PARALLEL DO (ω)

save $\widetilde{F}_{NL_2}(x,y,:)$ as $\widetilde{F}_{NL_1}(x,y,:)$

PARALLEL DO $x = x_{min}, x_{max}$

DO $y = y_{min}, y_{max}$

calculate electron density $\rho(x,y,:)$! : denote t

calculate nonlinear term $\widetilde{F}_{NL_2}(x,y,:)$! : denote ω

END DO (y)

END PARALLEL DO (x)

PARALLEL DO $\omega = \omega_{min}, \omega_{max}$

calculate spectra $\widetilde{\varepsilon}(x,y,\omega)$ by Eq. (6) !stepsize= $\Delta z/2$

END PARALLEL DO (ω)

save $\widetilde{F}_{NL_2}(x,y,:)$ as $\widetilde{F}_{NL_1}(x,y,:)$

END DO (z)

! in the first z loop step, we have to use $\widetilde{F}_{NL_1}(x,y,:) = 0$

END PROGRAM

ACKNOWLEDGMENTS

This work was supported by the National Basic Research program (Contract No. 2011CB808100, 2010CB923203), the National Natural Science Foundation (Contracts No. 11104236, 11134010, 61008011, 61008061), Jiangsu Province Natural Science Foundation (Contract No. BK2010173), China Postdoctoral Science Foundation, Shanghai Science and Technology Talent Project (12XD1405200), and the Priority Academic Program Development of Jiangsu Higher Education Institutions (PAPD) of China.

[1] A. Braun, G. Korn, X. Liu, D. Du, J. Squier, and G. Mourou, Opt. Lett. **20**, 73 (1995).

[2] Filamentation publications at website: www.filamentation.org /Publications. aspx.

[3] G. Méchain, A. Couairon, M. Franco, B. Prade, and A. Mysyrowicz, Phys. Rev. Lett. **93**, 035003 (2004).

[4] G. Méchain, A. Couairon, Y.-B. André, C. Damico, M. Franco, B. Prade, S. Tzortzakis, A. Mysyrowicz, R. Sauerbrey, Appl. Phys. B **79**, 379 (2004).

[5] W. Liu, S. A. Hosseini, Q. Luo, B. Ferland, S. L. Chin, O. G. Kosareva, N. A. Panov, V. P. Kandidov, New J. Phys. **6**, 6 (2004).

[6] O. G. Kosareva, N. A. Panov, V. P. Kandidov, Atmos. Oceanic Opt. **18**, 204 (2005).

[7] S. A. Hosseini, Q. Luo, B. Ferland, W. Liu, S.L. Chin, O.G. Kosareva, N. A. Panov, N. Aközbek, V. P. Kandidov, AIP Conf. Proc. **748**, 198 (2005).

[8] S. Champeaux, L. Bergé, D. Gordon, A. Ting, J. Penano, and P. Sprangle, Phys. Rev. E **77**, 036406 (2008).

[9] P. Polynkin, M. Kolesik, E. M. Wright, and J. V. Moloney, Phys. Rev. Lett. 106, 153902 (2011).

[10] P. Panagiotopoulos, D. Abdollahpour, A. Lotti, A. Couairon, D. Faccio, D. G. Papazoglou, and S. Tzortzakis, Phys. Rev. A **86**, 013842 (2012).

[11] T.-T. Xi, X. Lu, and J. Zhang, Phys. Rev. Lett. **96**, 025003 (2006).

[12] J. Wu, Y. Tong, X. Yang, H. Cai, P. Lu, H. Pan, and H. Zeng, Opt. Lett. **34**, 3211 (2009).

[13] H. Cai, J. Wu, P. Lu, X. Bai, L. Ding, and H. Zeng, Phys. Rev. A **80**, 051802(R) (2009).

[14] L. Bergé, S. Skupin, F. Lederer, G. Méjean, J. Yu, J. Kasparian, E. Salmon, J. P. Wolf, M. Rodriguez, L. Wöste, R. Bourayou, and R. Sauerbrey, Phys. Rev. Lett. **92**, 225002 (2004).

[15] L. Bergé, M. R. Schmidt and J. J. Rasmussen, P. L. Christiansen and K. O. Rasmussen, J. Opt. Soc. Am. B, **14**, 2550 (1997).

[16] A. E. Siegman, *Lasers*, University Science Books, (1986).

[17] J. Liu, H. Schroeder, S. L. Chin, R. Li, W. Yu, and Z. Xu, Phys. Rev. A **72**, 053817 (2005).

[18] M. Mlejnek, E. M. Wright, and J. V. Moloney, Phys. Rev. E **58**, 4903 (1998).

[19] Z. Wang, C. Zhang, J. Liu, and Z. Xu, Opt. Express **20**, 9558 (2012).

[20] A. Couairon, E. Bramlilla, T. Corti, D. Majus, O. de J. Ramirez-Gongora, and M. Kolesik, Eur. J. Special Topics **199**, 5 (2011).

[21] J. W. Thomas, *Numerical Partial Differential Equations: finite difference methods*, Springer (1995).

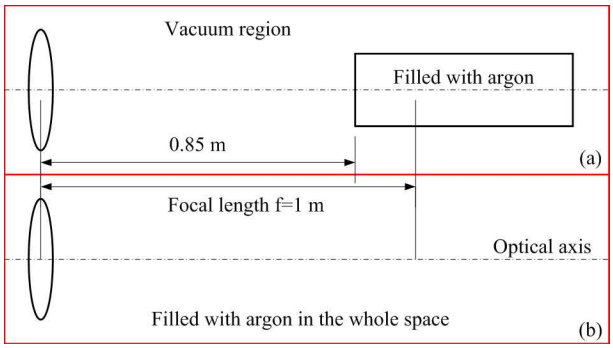

FIG. 1. Assumed setup sketch for our numerical experiment. The laser pulses incident from the left-side of the lens and the origin of the reference is located at the linear focus of the lens.

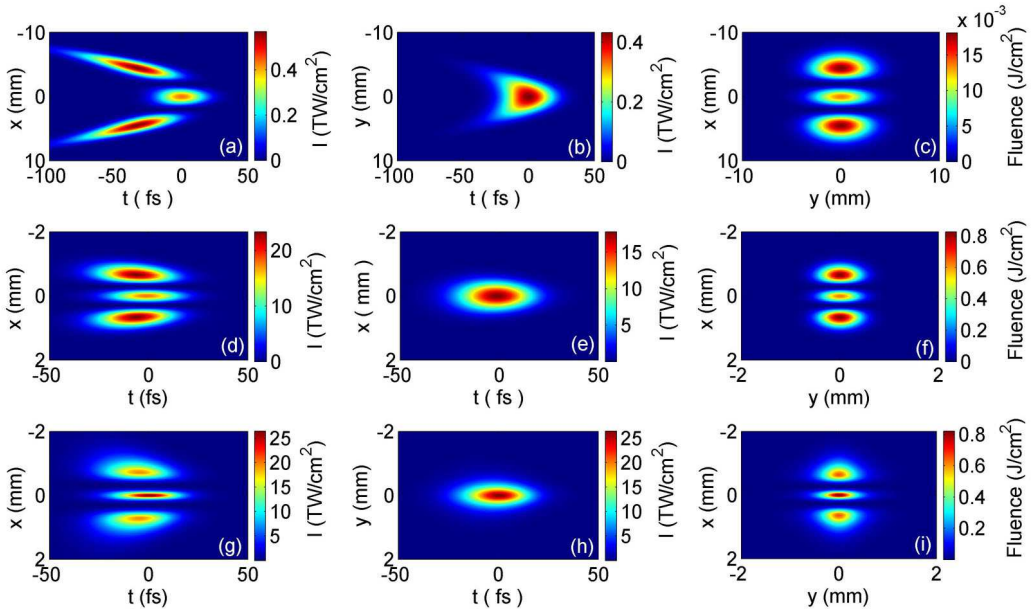

FIG. 2. (a,d,g) Laser pulse intensity in the *x*-*t* plane; (b,e,h) laser pulse intensity in the *y*-*t* plane; (c,f,i) fluence distribution calculated in terms of $\int |\varepsilon(x,y,t)|^2 dt$. (a,b,c) Correspond to the plane immediately behind the lens, evaluated from Eq. (2); (d,e,f) correspond to the distance 85.3 cm behind the lens, evaluated analytically by Eq. (8); (g,h,i) correspond to the same distance as in (d,e,f) but evaluated by numerically solving Eq. (3).

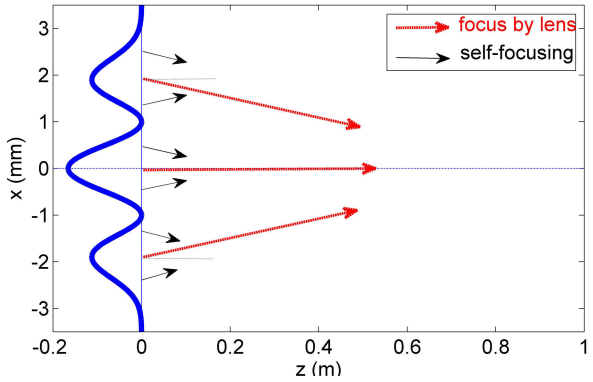

FIG. 3. Schematic diagram of the focus effect by lens and self-focusing due to nonlinearity for the three lobes of TEM_{02} HG mode in the *x*-*z* plane. The intensity curve used here correspond to $y = t = 0$ and $z = 50$ cm.

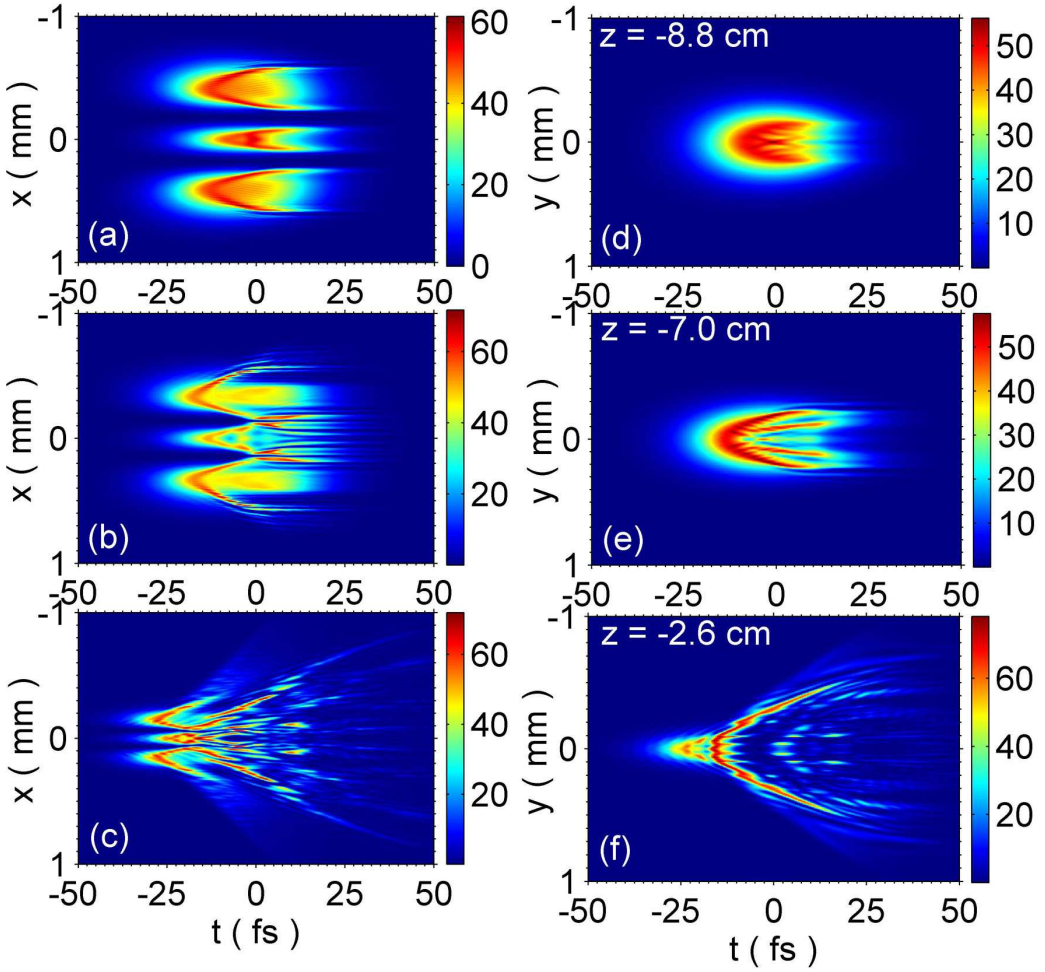

FIG. 4. Spatio-temporal intensity distribution at several typical distances, which is plotted from initial condition expressed in Eq. (8) at $z = -15$ cm. More details are shown in our media files (.GIF files).

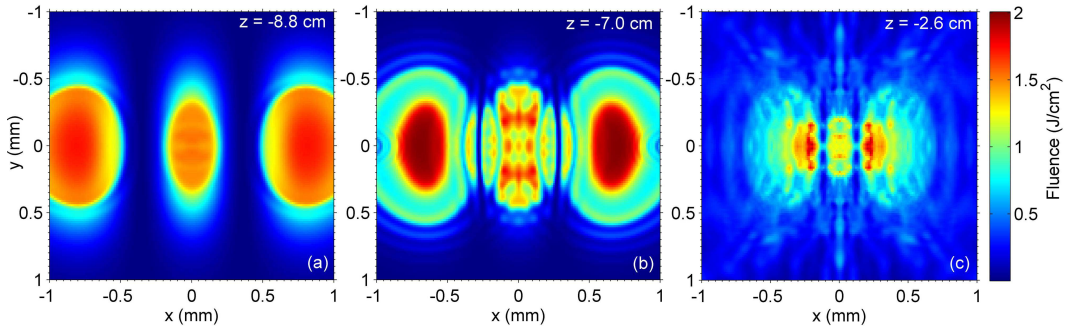

FIG. 5. (a,b,c) Fluence distributions in the *x*-*y* plane in several typical propagation distance corresponding to Fig. 4. The figure is plotted from the data obtained by numerically evaluating the Eq. (3) from initial condition expressed in Eq. (8) at $z = -15$ cm.

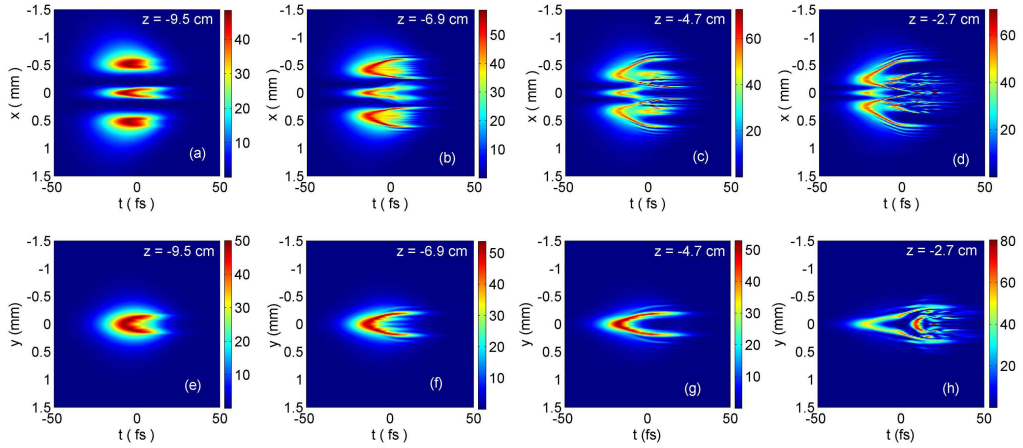

FIG. 6. Spatio-temporal intensity distribution at several typical distances, which is plotted from the data obtained by directly numerically evaluating the Eq. (3) from initial condition expressed in Eq. (2) where $z = -100$ cm.

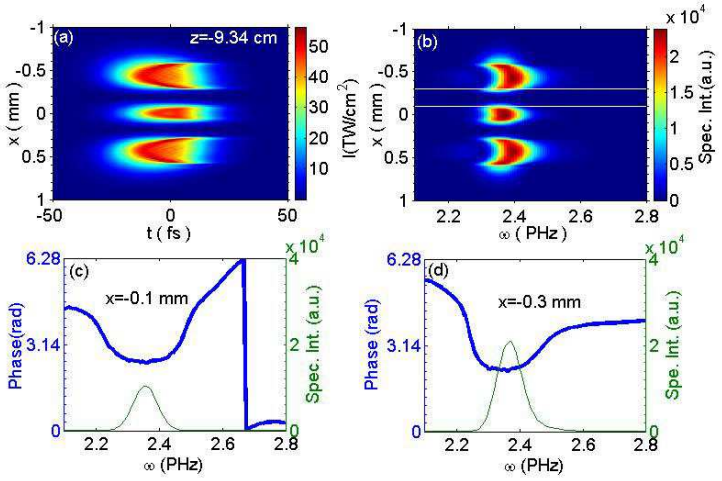

FIG. 7. (a) Spatio-temporal intensity distribution in the *x*-*t* plane and (b) spectral intensity distribution in the *x*-*ω* plane at $z = -9.34$ cm.(c,d) Spectral intensity (green thin line) and phase (blue thick line) at $x = -0.1$ mm and $x = -0.3$ mm, corresponding to $z = -9.34$ cm as marked in (b).

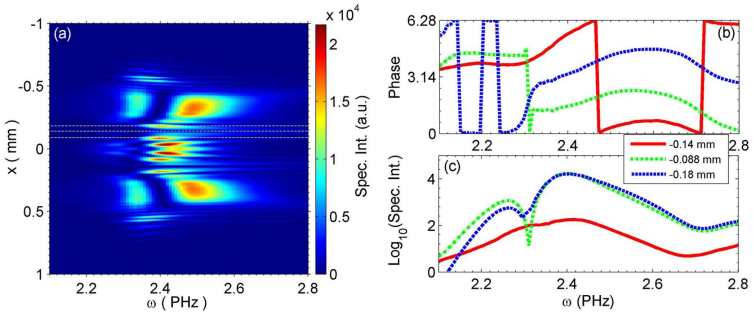

FIG. 8. (a) Specral intensity distribution in the *x*-*ω* plane at $z = -7.0$ cm, corresponding to Fig. 4(b). (b) Spectral phase and (c) spectral intensity at $x = -0.14$ mm, $x = -0.088$ mm and $x = -0.18$ mm.